TOPICAL REVIEW

Frequency Diverse Array SAR With Fast-Time Space-Time Adaptive Processing for Subsurface Imaging

WEN-QIN WANG, (Senior Member, IEEE)

Yangtze Delta Region Institute (Huzhou), University of Electronic Science and Technology of China, Huzhou 313001, China

e-mail: wqwang@uestc.edu.cn

ABSTRACT Different from the ground penetration radar providing only one-dimensional image, synthetic aperture radar (SAR) can produce two-dimensional and even three-dimensional image, which is meaningful in subsurface imaging, but possible layover effects may be a problem. Moreover, multipath reflections from the ground known as hot clutter or terrain scattered interferences will add nonstationary interference components to the subsurface imaging. In this paper, we present the use of fast-time space-time adaptive processing (STAP) to suppress undesired interferences for SAR subsurface imaging. Moreover, the frequency diverse array (FDA) range- and time-dependent beampattern is explored to enhance the SAR azimuth resolution and reduce fluctuations in the received signals, which helps in mitigating multipath effects and potentially addressing layover issues. The FDA-SAR platform moves at a constant speed along with the azimuth direction above the ground with a side-looking FDA antenna to formulate a strip-map side-looking SAR for subsurface imaging, where the FDA antenna elements also are placed along with the moving track of FDA-SAR platform. The research progress is reviewed and the most recent advances are introduced. The technical challenges and future works also are discussed. We aim to introduce the promising FDA-SAR with fast-time STAP for subsurface imaging and encourage further exploration in this domain.

INDEX TERMS Frequency diverse array, synthetic aperture radar, subsurface imaging, fast-time space-time adaptive processing, layover effect, multipath interference.

I. INTRODUCTION

Subsurface exploration is encountered in numerous applications [1], [2], [3], [4], [5], [6], such as oil-field and groundwater determination in deserts, archaeological survey, planetary exploration and landmine detection. There are also many other applications including detection of landmines and underground facilities. For instance, it was estimated that up to 110 million landmines need to be cleared, and more than 500 civilians are killed or maimed each week by landmines [7].Ground penetrating radar (GPR) is a typical technique for the aforementioned problems [8]. Although GPR is effective in detecting and discriminating subsurface objects, this requires a sensor being close to the ground,

as well as limited spatial coverage for large observation areas where climatic conditions are particularly hostile [9]. Synthetic aperture radar (SAR) potentially represents a major tool for subsurface exploration, since it provides a dense temporal and large spatial coverage due to much higher platform altitude than GPRs, ideally in all-weather operation. SAR mostly uses a wideband signal to ensure the range resolution, while improves the azimuth resolution via a long synthetic aperture. Thus, SAR can be a complementary technology to detect subsurface objects [10], even though it has a limitation in the imaging depth with respect to GPR. The advantages of SAR in subsurface imaging applications of is reflected in the increase of publications [11], [12], [13].

Although SAR is a well-known imaging technique, it is very sensitive to both additive noise and radio frequency (RF) interferences. In subsurface imaging applications, different

The associate editor coordinating the review of this manuscript and approving it for publication was Li He.

dielectric constants between the soil and air will bend the paths of electromagnetic wave at their interfaces. Moreover, multipath reflections from the ground known as hot clutter or terrain scattered interferences will add nonstationary interference components to produce degraded subsurface image. To address this problem, space-time adaptive processing (STAP) [14] can be adopted to suppress these undesired interferences while not significantly effecting the SAR imaging performance [15], [16], [17]. STAP is primarily used for array signal processing, which can effectively suppress interferences based on the assumption that the number of homogeneous sample supports is more than a double number of the array degrees-of-freedom (DOFs). This assumption may not be realistic in actual subsurface imaging applications due to intrinsic nonstationarity of the clutter, because both direct-path and multipath reflections may produce terrain scattered interference or hot clutter. Moreover, their performance will degrade dramatically in the presence of range ambiguity. More seriously, if a forward-looking SAR is considered, the simple Doppler sine-azimuth relationship no longer exists and there becomes a significant range-Doppler dependence, which will destroy the independently and identically distributed (iid) data assumption required in ideal STAP algorithms. As nonstationary interferences can be suppressed in a pulse-by-pulse way, fast-time STAP was suggested [15]. This paper investigates the use of fast-time STAP to suppress undesired multipath interferences for side-looking strip-map SAR subsurface imaging.

Furthermore, we use frequency diverse array (FDA) antenna in the SAR to provide range-, angle- and time-dependent beamforming to reject multipath interfering signals and suppress possible layover effects. FDA is a promising concept proposed by Antonik etal. in 2006 [18]. Different from traditional phased-array, multiple-input multiple-output (MIMO), frequency scanning array and orthogonal frequency division multiplexing (OFDM) techniques, FDA uses a small frequency offset, as compared to its carrier frequency, across the array elements. The comparisons between FDA and other similar techniques such as phased-array, MIMO, frequency scanning and time-modulated arrays are listed in Table 1. The FDA frequency offset results in a range-dependent beampattern for which the beam focusing direction will change as a function of the range, angle and even time. This provides both range-dependent and angle-dependent beampattern which enables the array beam to scan the space region without the need of phase shifters or mechanical steering. The multipath FDA characteristics analyzed in [19] show that FDA has the capability to form a quasi-flat interfering pattern for the desired ranges if its bandwidth is set properly. These properties make FDA potentially useful for the subsurface imaging applications with multipath interferences. The FDA range-dependent beampattern can be adopted to enhance the SAR azimuth resolution and reduce fluctuations in received signal, which helps in mitigating

multipath effects and potentially addressing layover issues (More details are provided in Section III. A).

In this paper, we jointly utilize SAR, STAP and FDA to formulate strip-map side-looking FDA-SAR with fast-time STAP for subsurface imaging. It was validated that forward-looking FDA-SAR can mitigate the Doppler-range relationship by reducing the amount of isodops [21], but we discuss mainly strip-map FDA-SAR. The FDA-SAR platform moves at a constant speed along with the azimuth direction above the ground with a side-looking FDA antenna to formulate a strip-map side-looking SAR for subsurface imaging, where the FDA antenna elements also are placed along with the moving track of FDA-SAR platform. The FDA can reduce the fluctuations of the received average power for multipath mitigation together with layover suppression and improve the azimuth resolution in SAR imaging. The FDA beamforming can be thought as a type of Doppler compensation to reduce the level of heterogeneous sample support data [22]. The decrease in deviation from the ideal iid assumption, namely, making the sample support data more homogeneous, can decrease the STAP degradation associated with interference covariance matrix estimation. Additionally, range-dependent interference suppression can be achieved by designing specific FDA range-dependent beampattern to illuminate the interfering rings different from that for the desired targets.

This paper focuses on the advancements in sensor technology and waveform design, rather than the image formation algorithms. The contribution lies in the advancement of SAR subsurface imaging by presenting a new FDA-SAR with fast-time STAP approach and encouraging further exploration in this domain. Recent advances in SAR subsurface imaging are presented, and potential applications together with the research challenges are discussed. The rest of this paper is organized as follows. Section II briefly introduces the basics and motivations for FDA-SAR subsurface imaging. Section III presents the STAP for the FDA-SAR subsurface imaging, followed by the performance analysis and discussions in Section IV. Technical challenges and future works in signal processing aspects are provided in Section V. Finally, concluding remarks are given in Section VI.

II. BASIC SAR, STAP AND FDA SCHEMES

In order to present the FDA-SAR with fast-time STAP subsurface imaging in a tutorial way, a brief introduction to basic SAR, STAP and FDA schemes are provided in this section.

A. BASIC SAR SCHEME

SAR usually employs a single physical antenna element to gather signals at different positions and different times. When the radar is carried on a platform, those positions are just functions of a single variable, distance along the radar platform moving track. When the acquired radar signals are

TABLE 1. Comparisons between FDA and several representative arrays.

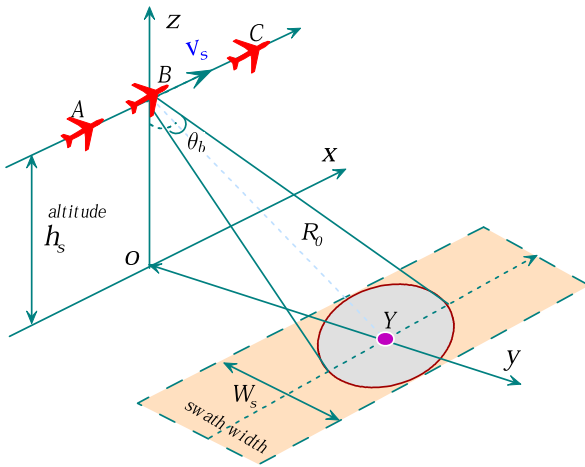| array name	subcarriers	transmitted signals	array gain	transmit beampattern	
				range-dependent	angle-dependent
FDA	non-orthogonal	coherent	√	√	√
phased-array	non-orthogonal	coherent	√		√
MIMO-OFDM	orthogonal	non-coherent			√
colocated MIMO	same carrier	non-coherent			√
frequency-scanning	same carrier	coherent	√		√
time-modulated	same carrier	coherent	√		√

FIGURE 1. Geometry of a side-looking strip-map SAR.

read out later and combined with specific phase shifts, the results are the same as if the recorded data have been gathered by an equally long and shaped phased-array radar. That is, the SAR simulates (rather than synthesizes) such a long phased-array radar.

In a basic strip-map SAR, the antenna collects the data while the radar platform is moving along with the azimuth direction.Figure 1 shows a side-looking strip-map SAR geometry with three radar positions, A, B, and C, together with a ground point target located at $(0, Y, 0)$. At radar position A, the radar beam begins to illuminate the target. At position B, the center of the radar beam is on the target. At position C, the radar beam ends the illumination on the target. Position B is chosen to be at $(0, 0, h_s)$, with beamwidth $\theta_b = \lambda/D_a$ (λ and D_a are the carrier wavelength and antenna length in azimuth, respectively) and h_s is the platform altitude. The distance between positions A and C is the physical synthetic aperture length, L_s, given by [23]:

$$L_s = R_0\theta_b = R_0\frac{\lambda}{D_a}, \qquad (1)$$

where R_0 is the closest distance between the target and radar.

As the radar platform moves, a swath W_s is mapped out on the ground by the antenna footprint. The radar transmits pulses at the pulse repetition frequency (PRF), and for each pulse the backscatter returned from the ground is sampled in the range at the analog-to-digital (A/D) sampling frequency. In doing so, the SAR range and azimuth resolutions are only

determined by its transmitted signal bandwidth and physical antenna length, respectively.

B. BASIC STAP SCHEME
The STAP, joint adaptive processing in the spatial and temporal domains, is a promising technique allowing the detection of targets with much smaller magnitude than competing ground clutter. The essence is to discriminate the target from competing ground clutter by exploiting the relationship existing between the spatial and temporal domains. One of the most important STAP characteristics is adaptivity, differentiating from the displaced phase center array (DPCA) processing [24], where the clutter rejection only is achieved through platform motion compensation.

Consider an M-element array radar transmitting a pulse in a certain direction angle. On receive, the snapshots of the returns collected by an N-element receiver at K successive time epochs give rise to the spatio-temporal nature of the received radar data. The spatio-temporal product NK is defined as the system dimensionality. That is, for a desired angle-Doppler looking direction, we can specify up to $NK-1$ "nulls". Figure 2 illustrates a basic schematic architecture of the STAP beamformer with N receiving elements and L pulse coherent processing intervals [14], [15]. The space-time beampattern can be formed by a judicious selection of the complex NK-dimensional weighting coefficient vector $\mathbf{w} = \text{vec}(w_1, \ldots, w_{NK})$ for the beamforming, with $\text{vec}(\cdot)$ being the vector operator. Fast-time STAP is an effective method to suppress the nonstationary scattered interference and offers the advantage of exploiting the coherence between various interfering scatters to achieve improved interference rejection performance.

C. BASIC FDA SCHEME
Figure 3 illustrates the comparisons between conventional phased-array and a standard FDA. The FDA involves modulating the same waveform to slightly different carriers for each transmitting element of the array. In a standard M-element FDA, the center frequency for the mth element is

$$f_m = f_0 + m\Delta f, \qquad m = 0, 1, \ldots, M-1, \qquad (2)$$

where f_0 and Δf denote the center frequency for the reference element and frequency offset, respectively. Unless state otherwise, a positive Δf is assumed in this paper.
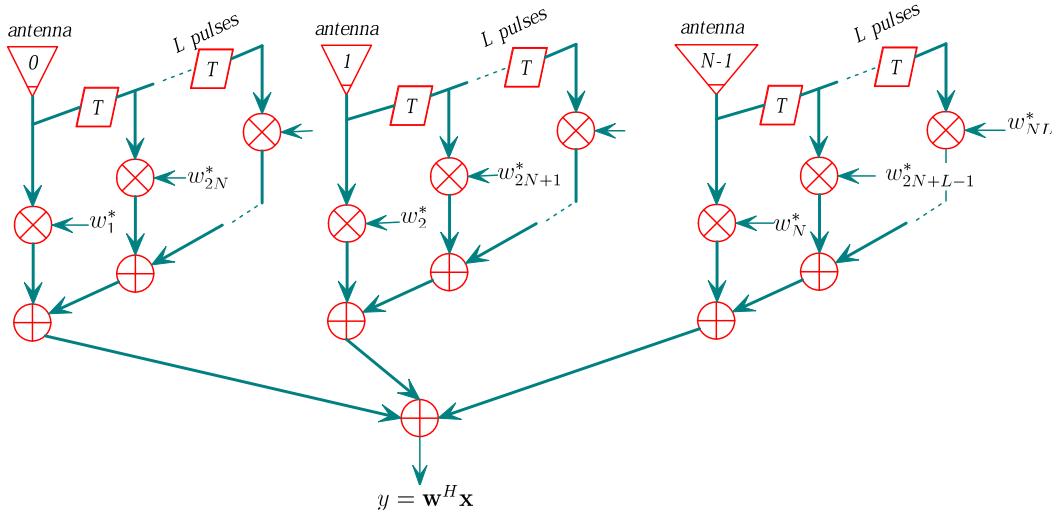
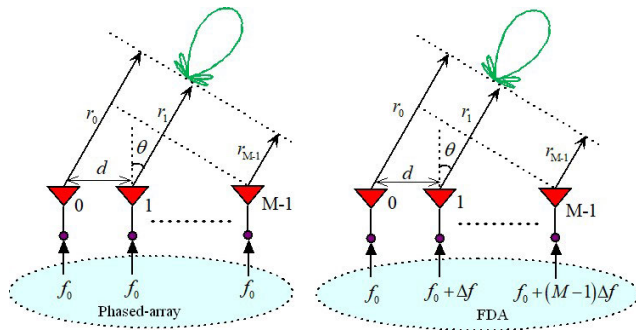**FIGURE 2.** Space-time beamformer consisting of *N* channels and *L* pulses.

FIGURE 3. Illustrative comparisons between phased-array and standard FDA transmitters.

The FDA electric field at the observation point **r** can be expressed as

$$E\left(\mathbf{r}, t\right) = \sum_{m=0}^{M-1} \frac{a_m}{r_m} \xi_m(\theta|\omega_m) e^{j2\pi\left(f_m\left(t - \frac{r_m}{c_0}\right)\right)}, \qquad t_s \le t \le t_e, \tag{3}$$

where c_0 is the speed of light, $\omega_m = 2\pi f_m$ is the angular frequency, a_m is the complex excitation coefficient for the mth element, t_s and t_e are the starting and ending times, respectively, and $T_p = t_e - t_s$ is the pulse duration. r_m is the slant range, θ is the angle from the normal with respect to the axis of the array and $\xi_m(\theta|\omega_m)$ is the far-field radiation pattern for the mth element that accounts for the direction and frequency dependence of the element's electric field.

In order to get a closed-form expression, in amplitude sense the distance differences md between individual antenna elements can be ignored, i.e., $r_m \approx r$. However, in phase sense, r_m can be approximated by $r_m = r - md\sin\theta$, with d being the element spacing. In addition, since $f_0 \gg \Delta f$, we have $\xi_m(\theta|\omega_m) \approx \xi_0(\theta|\omega_0)$, where $\omega_0 = 2\pi f_0$.

Accordingly, (3) can be reformulated as

$$E\left(\mathbf{r}, t\right) \approx \frac{\xi_0(\theta|\omega_0)}{r} e^{j\omega_0\left(t - \frac{r}{c_0}\right)}$$
$$\times \sum_{m=0}^{M-1} a_m e^{jm\left(2\pi\Delta f\left(t - \frac{r}{c_0}\right) + \omega_0 \frac{d\sin\theta}{c_0}\right)}. \tag{4}$$

Note that, due to the fact that $r \gg (M-1)d\sin\theta$ and $f_0 \gg \Delta f$, the term $m2\pi\Delta fd\sin\theta/c_0$ is ignorable, where c_0 is the speed of light. Specifically, if equal $\{a_m\}$ are assumed, the FDA transmit beampattern can be derived as [25]

$$P(\theta, r, t) = \left| \frac{\sin\left(M\pi\left(\Delta ft - \frac{f_0}{c_0}r + \frac{f_0+\Delta f}{c_0}d\sin\theta\right)\right)}{\sin\left(\pi\left(\Delta ft - \frac{f_0}{c_0}r + \frac{f_0+\Delta f}{c_0}d\sin\theta\right)\right)} \right| \tag{5}$$

This implies that the FDA beampattern will depend on the angle θ, range r and even time t, not just only the angle in phased-array beampattern.

Assuming the following parameters: $M = 32$, $\Delta f = 1kHz$, $d = c_0/2f_0$ and $r = 120km$, Fig. 4 compares the FDA transmit beampatterns under continuous-wave and pulsed transmissions, with $t_s = 1ms$ and $T_p = 1/(5 \cdot \Delta f)$ for the pulsed-FDA simulation. The continuous-FDA has a continuous beampattern with the scanning periodicity of $1/\Delta f$. Similar to conventional phased-array, if $d < c_0/2f_0$ is chosen, there will have no grating lobes [22]. The pulse transmitted at $t_s = 1ms$ forms a scanning beam at the time of $t_s + r/c_0 = 1.4ms$ with an apparent angle drift about $30°$, from $4°$ at $1ms$ to $-26°$ at $1.4ms$. Obviously, similar phenomenon can be observed at different distances except that the starting time is delayed accordingly.

III. STAP FOR FDA-SAR SUBSURFACE IMAGING
A. MOTIVATION
High resolution in both range and azimuth dimensions are meaningful to image the subsurface objects that are
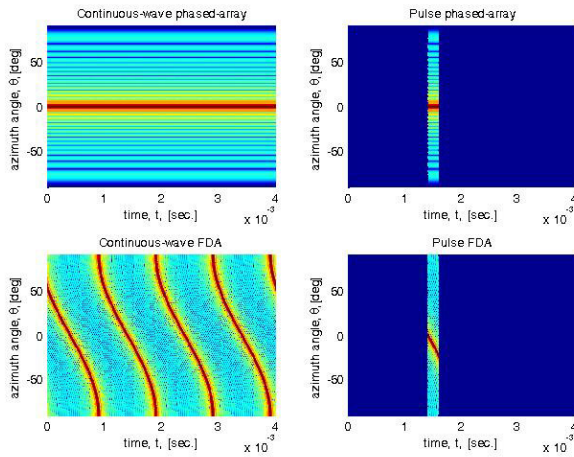
FIGURE 4. Beampattern comparison between phased-array and FDA under continuous-wave and pulse waveforms: (a) continuous phased-array, (b) pulsed phased-array, (c) continuous FDA, (d) pulsed FDA.

usually far smaller than conventional radar targets. If a real aperture radar is adopted, a high carrier frequency or large antenna is required. In subsurface radar applications, a relatively low frequency below 1 GHz should be adopted; Otherwise, serious signal attenuation will be caused by the soil's low-pass electromagnetic propagation effects. Even at the frequency of 1 GHz, an 18-meter antenna is required to achieve an azimuth resolution of 1 degree. Certainly, it is not acceptable for subsurface imaging applications, where conveniently movable antenna and easy operation are strongly desired. SAR can achieve high azimuth resolution for subsurface imaging, but conventional SAR for subsurface imaging requires a long collection time and even results in image smearing effects.

Moreover, different from conventional airborne and space-borne SAR systems, in practical SAR subsurface imaging applications, distinct dielectric constants between the soil and air will bend the electromagnetic wave propagation path at their interfaces. Moreover, SAR subsurface imaging performance may be seriously degraded by the multipath propagation effects in complex subsurface mediums. Extending SAR operations from a single antenna to array antenna operation offers many benefits including improved ambiguity suppression and improved signal-to-noise ratio (SNR). But the majority of literature relating to array antenna SAR utilizes phased-array antenna. A newer concept is to adopt FDA antenna for SAR imaging. Farooq [26] has made an attempt to exploit the FDA increased apparent beamwidth to improve azimuth resolution while retaining the benefits of shorter synthetic aperture and integration time. Inspired also by the FDA range-dependent and time-variant beam-pattern, we adopt FDA-SAR to handle the multipath, range-ambiguous clutter and even layover problems in subsurface imaging.

For SAR subsurface imaging, the frequency progression can be applied in both elevation and azimuth dimensions.

For illustration simplicity and without loss of general-ity, Fig. 5 illustrates a linear-array FDA-SAR subsurface imaging geometry, where the FDA-SAR platform moves at a constant speed along the azimuth direction above the ground with a side-looking FDA antenna to formulate a strip-map SAR subsurface imaging, and the FDA antenna elements also are placed along the moving track of the FDA-SAR platform. That is, the FDA antenna elements are placed along the azimuth direction, not the elevation direction. Figure 5(a) compares FDA-SAR physical synthetic aperture half-beamwidth $\Delta\theta$ and equivalent apparent half-beamwidth $\Delta\theta_{app}$. Since the traditional phased-array beam is both range-independent and time-independent, its beam propagation path from the radar platform to the imaging target is a direct-line. Differently, according to (5), due to the range- and time-dependent beampattern characteristics, even for a given fixed physical direction θ, the FDA will generate an apparent direction θ_a [25]:

$$\theta_a = \arcsin\left(\frac{c_0\Delta f t}{2\pi f_0 d} + \sin\theta + \frac{\Delta f \sin\theta}{f_0} + \frac{\Delta f r}{f_0 d}\right) \quad (6)$$

The apparent direction θ_a is different from its real physical direction θ, which implies that FDA apparent direction depends on not only its physical direction but also the employed frequency offset Δf and range r. This states that even for a given fixed physical direction angle, the FDA apparent beam will be bended due to its range-dependent interferometrically propagation effects. As a consequence, the equivalent apparent FDA aperture beam will be extended from u to u_{app}. Accordingly, the FDA-SAR physical synthetic aperture half-beamwidth will be extended to the equivalent apparent synthetic aperture half-beamwidth. That is to say, the range-dependent beampattern of FDA can enlarge the synthetic aperture length from $\Delta\theta$ to $\Delta\theta_{app}$ and accordingly improve the SAR azimuth imaging resolution.

Figure 5(b) is just a multipath illustration, where a bistatic geometry is drawn to clarify the purpose. Fig. 5(c) illustrates subsurface SAR refraction effect between air dielectric constant ε_a and soil dielectric constant ε_b. In a traditional non-FDA SAR, the radar interrogates the scene at a certain aspect angle $\Delta\theta$ as measured from the synthetic aperture normal. By introducing FDA, it is envisioned that the data will be collected by the resultant "bent beam" at each point along the synthetic aperture. The data collected at the azimuth position u will be projected to an apparent collection point u_{app} located at an apparent aspect $\Delta\theta_{app}$ [26]. If the FDA frequency offsets are adaptively varied at each collection point, such that the FDA maintains its bent beam focused at the scene center, the locus of apparent collection locations will form an apparent synthetic aperture with length L_{app}, which is obviously longer than its physical synthetic aperture length L_s. This implies that higher azimuth resolution can be achieved for the FDA-SAR than a conventional phased-array SAR.
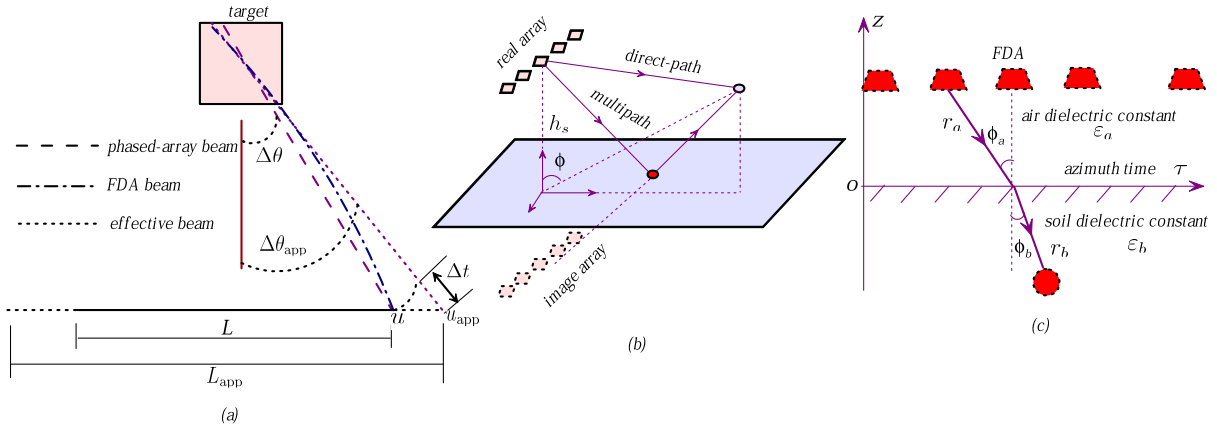
FIGURE 5. Geometries for FDA-SAR subsurface imaging: (a) FDA SAR physical angle and apparent angle; (b) Illustration of FDA multipath propagation, where a bistatic geometry is shown; (c) Illustration of subsurface SAR refraction effects.

Under a far-field condition, analogous to (3), the direct-path component of the FDA electric field at the observation point **r** can be expressed as [19]

$$E_d (\mathbf{r}, t) = \sum_{m=0}^{M-1} a_m \xi_m (\theta_{dm}, \phi_{dm} | \omega_m) \frac{e^{j\omega_m(t-(r-mdu-h_sv)/c_0)}}{r},$$
$$(7)$$

where m and d in all subscripts denote for the mth element and direct-path propagation component, respectively, and $u = \sin\phi\cos\theta$ and $v = \cos\phi$ represent the directional cosines, with θ and ϕ being the azimuth and elevation angles with respect to the observation point, respectively.

According to the SAR imaging principle, the reflected components can be equivalently represented by the signal emanated from the FDA-SAR located at a depth of h_s (equal to the platform altitude) below the ground plane. That is,

$$E_r (\mathbf{r}, t) = -\sum_{m=0}^{M-1} a_m \xi_m (\theta_{rm}, \phi_{rm} | \omega_m) \frac{e^{j\omega_m(t-(r-mdu+h_sv)/c_0)}}{r}.$$
$$(8)$$

Although SAR subsurface imaging may be influenced by many hardware and environmental factors during data collection such as transmit power, soil properties, electric constant, electromagnetic reflection coefficient and even polarization of the signal, the SAR image reconstruction relies solely on the target radar cross section (RCS) and phase information in a scattered pulse return, Other amplitude and phase contributions are approximately constant in data collection and provide no target information. Therefore, due to the fact that $h_s \ll r$ and $md \ll r$, which implies that both θ_{dm} (θ_{rm}) and ϕ_{dm} (ϕ_{rm}) are small, we have $\xi_m (\theta_{dm}, \phi_{dm} | \omega_m) \approx \xi_m (\theta_{rm}, \phi_{rm} | \omega_m) \approx \xi_0 (\theta, \phi | \omega_0)$.

For a uniform linear array with M elements excited by uniform amplitudes, namely, $a_m = 1$, the total electric field including both direct-path and reflection-path components at

the observation point **r** can be expressed as

$$E_{\text{tot}} (\mathbf{r}, t) = E_d (\mathbf{r}, t) + E_r (\mathbf{r}, t)$$
$$= \frac{\xi_0 (\theta, \phi | \omega_0)}{r} e^{j\left[\omega_0\left(t-\frac{r}{c_0}\right) - \frac{\delta\omega((M-1)/2)^2 du}{c_0}\right]}$$
$$\times \left\{ e^{j\omega_0 h_s v/c_0} \frac{\sin\left(M\frac{\Psi^d}{2}\right)}{\sin\left(\frac{\Psi^d}{2}\right)} \right.$$
$$\left. + e^{-j\omega_0 h_s v/c_0} \frac{\sin\left(M\frac{\Psi^r}{2}\right)}{\sin\left(\frac{\Psi^r}{2}\right)} \right\},$$
$$(9)$$

with $\delta\omega = 2\pi\Delta f$, $\Psi^d = \frac{\omega_0 du}{c_0} + \delta\omega\left(t - \frac{r+(N-1)du-h_sv}{c_0}\right)$ and $\Psi^r = \frac{\omega_0 du}{c_0} + \delta\omega\left(t - \frac{r+(N-1)du+h_sv}{c_0}\right)$. Note that $E_r (\mathbf{r}, t)$ includes both ground and subsurface objects. Since the total electric field $E_{\text{tot}} (\mathbf{r}, t)$ also exhibits a time-variant pattern, we can adopt the averaged receiver power as a metric [19]:

$$P_{\text{avg}} (\mathbf{r}) \triangleq \frac{1}{T} \int_T |E_{\text{tot}} (\mathbf{r}, t)|^2 \, dt$$
$$\approx 2\frac{|\xi_0 (\theta, \phi | \omega_0)|^2}{r^2}$$
$$\times \left[M - \cos\left(\frac{2\omega_0 h_s v}{c_0}\right) \frac{\sin\left(\frac{M\delta\omega h_s v}{c_0}\right)}{\sin\left(\frac{\delta\omega h_s v}{c_0}\right)} \right]. \quad (10)$$

As shown in Fig. 6, where $\chi = 2\pi f_0 h_s \cos\phi/c_0$ is a normalized parameter, FDA reduces the fluctuations of the received signal average power, which is mainly attributed to distinct null/maxima ranges corresponding to different frequency components radiated by the FDA. That is, FDA can form a quasi-flat interference pattern for the desired ranges. Those properties make FDA potentially outperforms phased-array in multipath propagation and layover suppression, which are particularly useful for subsurface imaging. Otherwise, the subsurface imaging performance might be degraded for a phased-array due to layover effects
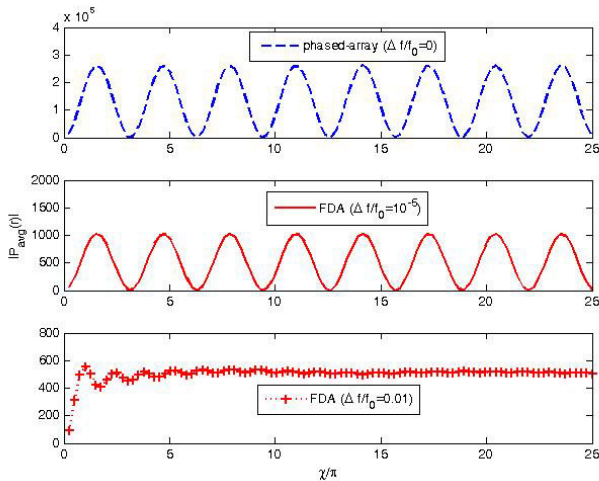
FIGURE 6. Comparisons of averaged receiver power versus the normalized parameter $\chi = 2\pi f_0 h_s \cos\phi/c_0$.

and range-dependent fading effects. More demonstrations between FDA and phased-array can be found in [19].

B. FAST-TIME STAP FOR FDA-SAR SUBSURFACE IMAGING

Different from airborne SAR and spaceborne SAR imaging, SAR subsurface imaging should exploit both direct-path and multipath reflections from the subsurface objects. Due to the platform motion, the spatial nulling for suppressing nonstationary multipath interferences should be carried out in a pulse-by-pulse basis. Nevertheless, it is not a straightforward problem by using fast-time STAP technique to remove the scattered interferences in the received subsurface signal. Normal STAP imposes a single constraint in the adaptive SAR beam but allows variations in the beampattern depending on the differences in the direction and strength of scattered interferences from pulse to pulse. For strong interferences in subsurface imaging, these variations may severely degrade the imaging performance [15]. One potential way to mitigate this problem is to jointly utilize FDA antenna and fast-time STAP to maintain the SAR beampattern from pulse to pulse.

It is easily understood from (3) that, even if the time variable t is fixed, the FDA beampattern is coupled in the range and angle dimensions, caused by the synchronous linearly changing between frequency offset and element spacing. If this synchronization is damaged, the FDA may yield uncoupled range-angle beampattern. Hence, we have two-type potential solutions: One is to use a linear array, and the other one is to adopt uniform linear array and nonlinearly increasing frequency offsets. Random frequency offsets [27], i.e., the second-type solution, are used in this paper to produce uncoupled range-angle beampattern for the FDA-SAR imaging.

The FDA-SAR gathers its data as it moves on or above the ground at some speed with a side-looking FDA antenna to formulate strip-map SAR subsurface imaging, which

transmits a stream of radar pulses and records the returned signals corresponding to each pulse. Similar to a phased-array radar, all FDA elements transmit the same baseband waveform in a pulsed way, i.e., the baseband signal for each element is $u(t), 0 \le t \le T_p$. The M-element FDA transmitted signal can be expressed as

$$s(t) = \sum_{m=0}^{M-1} a_m u(t) \exp\left(j2\pi \left(f_0 + \Delta f_m\right) t\right), \quad (11)$$

where Δf_m denotes the frequency offset for the mth element. The signals received by the nth channel of the FDA-SAR include the desired object return $s_{r_n}(t, \tau)$, the undesired multipath interference $q_n(t, \tau)$ and unavoidable receiver noise $v_n(t, \tau)$:

$$x_n(t, \tau) = s_{r_n}(t, \tau) + q_n(t, \tau) + v_n(t, \tau), \quad (12)$$

where τ denotes the slow-time (azimuth time). Using the "stop-and-go" assumption, all signals received by the N-channel receiver can be formulated as a vector

$$\mathbf{x}(t, \tau) = [x_1(t, \tau), \ldots, x_N(t, \tau)]^T, \quad (13)$$

with ^{T} being the transpose operator.

A spatial adaptive beamforming can be performed to correctly evaluate the response for each focusing position. The fast-time beamforming output is given by

$$\mathbf{y}(t, \tau) = \mathbf{w}^H(\tau)\mathbf{x}(t, \tau), \quad (14)$$

with ^{H} being the conjugate transpose operator. The azimuth time dependent weight vector should be designed to minimize the mean square value of the undesired signal component at each pulse subject to a set of constraints. In order to minimize the interference-plus-noise power and maintain a distortionless response towards the direction of the interested target, adaptive processing in fast-time dimension is applied. The $\mathbf{w}(\tau)$ can be obtained by the minimum variance distortionless response (MVDR) criterion [28]:

$$\min_{\mathbf{w}(\tau)} \mathbf{w}^H(\tau)\mathbf{R}_{i+n}(\tau)\mathbf{w}(\tau)$$
$$\text{s.t. } \mathbf{w}^H(\tau)\mathbf{s}_r(t, \tau) = 1, \quad (15)$$

where $\mathbf{R}_{i+n}(\tau)$ is the ideal interference-plus-noise covariance matrix and $\mathbf{s}_r(t, \tau) = \left[s_{r_1}(t, \tau), \ldots, s_{r_N}(t, \tau)\right]^T$ is the desired object vector. The $N \times 1$ weight vector is solved as

$$\hat{\mathbf{w}}(\tau) = \frac{\mathbf{R}_{i+n}^{-1}(\tau)\mathbf{s}_r(t, \tau)}{\mathbf{s}_r^H(t, \tau)\mathbf{R}_{i+n}^{-1}(\tau)\mathbf{s}_r(t, \tau)}, \quad (16)$$

where $^{-1}$ denotes the inverse of a matrix. Oftentimes, the matrix $R_{i+n}(\tau)$ is unavailable and, therefore, the sample covariance matrix which is obtained by averaging over Q training data: $\hat{\mathbf{R}}_{i+n}(\tau) \triangleq \frac{1}{Q} \sum_{q=1}^{Q} \mathbf{y}(q, \tau)\mathbf{y}^H(q, \tau)$. In typical operations, the training data $\mathbf{y}(q, \tau), q = 1, 2, \ldots, Q$ are obtained using the radar returns from the angle-time bins adjacent to the angle-time bin of interest. Undesired

interferences can be suppressed by this fast-time adaptive beamforming in a pulse-to-pulse way. Therefore, in doing so, interference-free signal model is considered in subsequent imaging algorithm discussions.

Since conventional Fourier transform algorithms for airborne and spaceborne SAR imaging are no longer valid for SAR subsurface imaging due to the fact that the objects exist the near-field of the SAR antenna in subsurface imaging, we can use the multiple scatter-point localization technique [29] to produce a focused SAR image. Suppose the object is composed of P scatters. Then the nth receiving channel signal from the P scatters, at a distance $R_{pn}(\tau)$ at the azimuth time τ, is

$$s_{r_n}(t, \tau) = \sum_{p=1}^{P} \sigma_p s \left(t - \frac{2R_{pn}(\tau)}{c_0} \right)$$
$$\times \exp \left(-j2\pi f_0 \frac{2R_{pn}(\tau)}{c_0} \right) + v_n(t), \quad (17)$$

with σ_p being the pth scatter's RCS. Subsurface imaging is equivalently to estimate the object RCS from the received signals at U azimuth positions, i.e., $\{\tau_u, u = 1, 2, \ldots, U\}$. Suppose the noise $\{v_n(t), n = 1, 2, \ldots, N\}$ are independent and identically Gaussian distributed, the maximum-likelihood (ML) estimation of the object RCS can be estimated by minimizing the following function:

$$J = \sum_{u=1}^{U} \int \left| s_{r_n}(t, \tau_u) - \sum_{p=1}^{P} \sigma_p s \left(t - \frac{2R_{kn}(\tau_u)}{c_0} \right) \right.$$
$$\left. \cdot \exp \left(-j2\pi f_0 \frac{2R_{kn}(\tau_u)}{c_0} \right) \right|^2 dt. \quad (18)$$

The object RCS can be estimated by minimizing J with the point-to-point correlation (PPC) method as follows [30]

$$\hat{\sigma}_p = \frac{1}{UE} \sum_{u=1}^{U} \int s_{r_n}(t, \tau_u) s_{r_n}^* \left(t - \frac{2R_{pn}(\tau_u)}{c_0} \right)$$
$$\cdot \exp \left(j2\pi f_0 \frac{2R_{pn}(\tau_u)}{c_0} \right) dt, \quad (19)$$

where $E = \int_{T_p} |s(t)|^2 dt$ is the transmitted energy in one pulse. It means that the essence of this method lies in the matched filtering for the received signals. When the matched-filter only matches the supposed scatter and mismatches any other scatters, we can successfully distinguish different scatters and estimate their parameters. Using the linearly frequency modulation (LFM) waveform with the bandwidth $B_r = 30MHz$ and chirp rate $k_r = 3 \times 10^{12}$, Fig. 7 shows that the FDA using random frequency offsets provides better radar ambiguity function characteristics than the standard FDA, at a cost of degraded Doppler tolerance, where normalized modulus amplitude is applied. Note that Fig. 7 is not merely to display the basic waveform characteristics, because the used signals in the ambiguity function has considered not only the basic waveform $u(t)$, but also frequency offset Δf_m related frequency modulation
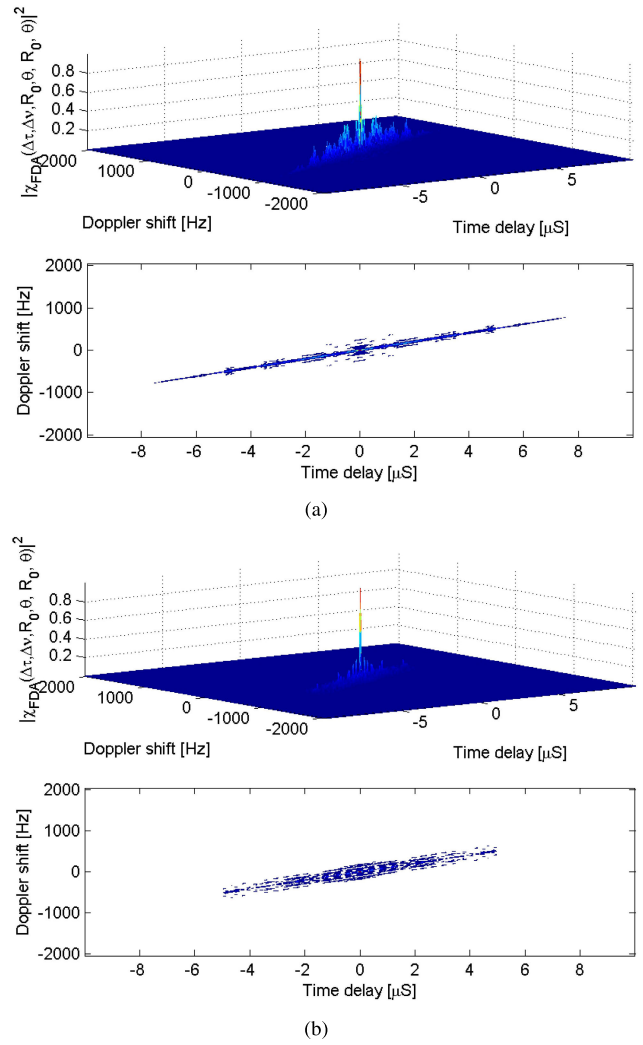

FIGURE 7. Comparisons of radar ambiguity function for LFM waveform: (a) standard FDA, (b) random FDA.

term $\exp(j2\pi(f_0 + \Delta f_m)t)$ and array element weightings a_m, as given in (11).

Figure 8 plots the signal processing chain from FDA signal transmission, fast-time STAP and PPC estimation-based image formulation [15]. First, the M-element FDA transmitter sends out radar pulse signal to the radar surface objects. Next, the N-element receiving antenna will receive the objects reflected returns and multipath interferences, clutter and noise. Then, the fast-time STAP will be applied to the baseband sampling signals to suppress undesired interferences and focus the object scatters in the fast-time (elevation) dimension. Next, the PPC estimation algorithm will be used to estimate the object scatters in the slow-time (azimuth) dimension. The PPC method [30] is a simplification of the ML algorithm. In far-field cases, it can be implemented through fast Fourier transform, but the Fourier transforms are not suitable for near-field subsurface objects. As a consequence, the PPC method should be performed to every supposed scatter. Accordingly, precision

TABLE 2. Target impulse response function between FDA-SAR and phased-array SAR.

	Azimuth resolution	Range resolution	Azimuth ISLR	Range ISLR
FDA	0.17 m	0.28 m	-9.72 dB	-9.70 dB
Phased-array SAR	0.19 m	0.30 m	-9.74 dB	-9.78 dB
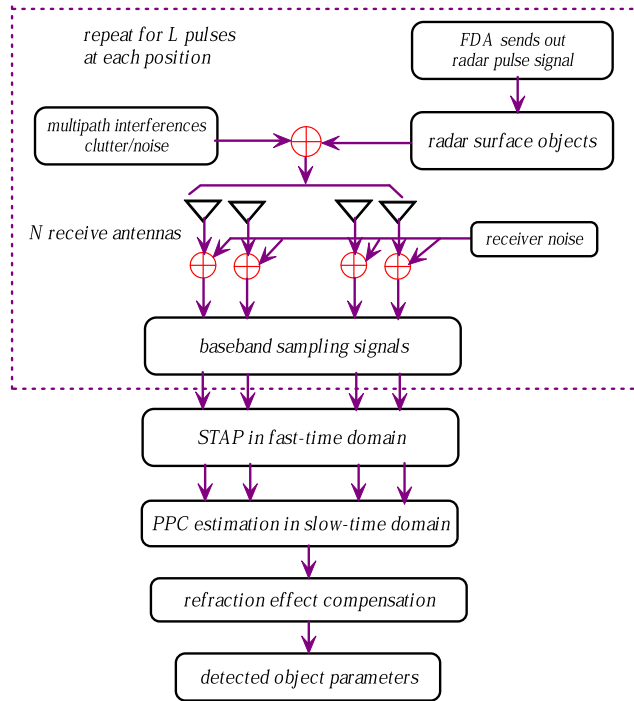
FIGURE 8. Signal processing chain for the FDA-SAR imaging.

FIGURE 9. Numerical imaging results for the scenarios with one desired object and two multipath interfering scatters. The multipath interference suppression is applied in the bottom one, but it not applied in the upper one.

FIGURE 10. Comparisons of target impulse response function between FDA-SAR and phased-array SAR.

position of the FDA antenna is required in the reflectivity estimation. Considering the signal model (10) and assuming the following parameters: $h_s = 1m$, $f_0 = 1GHz$, $B_r = 100MHz$, $T_p = 10\mu s$, $M = N = 16$ and $\Delta f = 1kHz$, Figure 9 gives the imaging results for the scenarios with one desired object located at $(2m, 0)$ (the former represents the position in range dimension, while the latter means the position in azimuth dimension) and two multipath interfering scatters located at $(2.072m, 0)$ and $(2.048m, 0)$ which RCS ratios to that of the objets are 0.5 and 0.25, respectively. Note that, according to the signal processing chain in Fig. 8, the multiple scatter-point localization technique [29] and the PPC method [30] are applied in the slow-time dimension after the application of the fast-time STAP in the elevation dimension. It is seen that, without the multipath interference suppression, ghost will be produced in the subsurface SAR image.

Additionally, suppose the following parameters: $R_0 = 100m$, $f_0 = 1GHz$, $B_r = 500MHz$, $\Delta\theta = 6°$, $M = N = 32$ and $\Delta f = 200kHz$, Figure 10 compares the target impulse response function between FDA-SAR and phased-array SAR. Their numerical imaging performance are compared in Table 2. The results show that the FDA achieves better imaging resolution in both range and azimuth
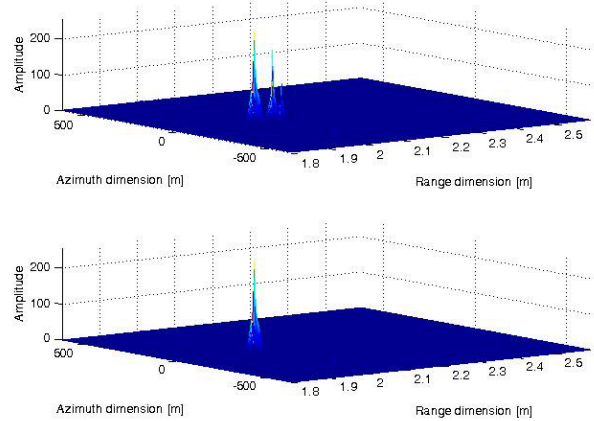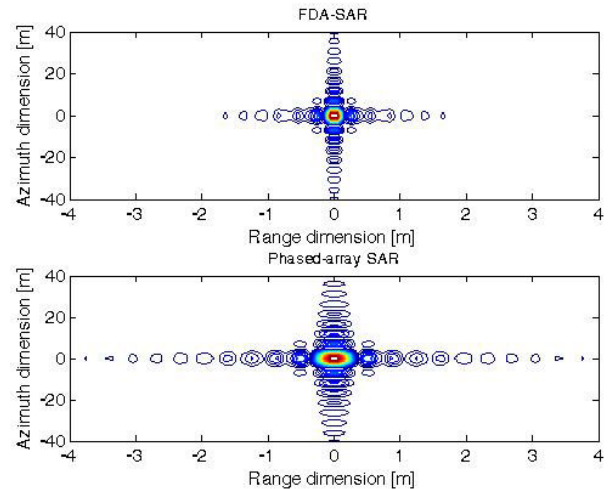
dimensions at a cost of slightly increased integrated sidelobe ratio. Note that, in Table 2 the azimuth resolution is improved better due to the fact that a relative small frequency offset is used in the simulation. Farooq et al. [31] derived that, given a linear FDA when the physical spatial scanning angle is $0°$, the apparent scanning angle will be $\arcsin\left(\frac{2R_0\Delta f}{c_0}\right)$. As expected, the range resolution is significantly improved while the azimuth resolution is slightly improved. The azimuth resolution can be further improved by increasing R_0 and/or Δf.

IV. PERFORMANCE ANALYSIS AND DISCUSSIONS

A. REFRACTION EFFECT COMPENSATION

While compared with conventional SAR surface imaging, SAR subsurface imaging has a specific difference lies that refraction effects will occur when the electromagnetic wave propagates from one medium to another one with different dielectric constants. Tomographic technique and angular diversity discussed in [32] can be adopted to deal with the refraction effects in subsurface SAR imaging. However, due to the fact that FDA time-variant beampattern will result in apparent time advances or time delays in the FDA-SAR returned data model, the refraction effects compensation should be applied with the consideration of FDA-SAR characteristics.

According to the Snell law and the geometry relation illustrated in Fig. 5, the unknown r_a, r_b, ϕ_a and ϕ_b can be obtained by solving the following equations [30]:

$$\frac{\sin \phi_a}{\sin \phi_b} = \sqrt{\varepsilon_r} \tag{20a}$$

$$r_a \sin \phi_a + r_b \sin \phi_b = x_b - x_a \tag{20b}$$

$$r_a \cos \phi_a = y_a \tag{20c}$$

$$r_b \cos \phi_b = -y_b, \tag{20d}$$

where ε_r is the medium's relative dielectric parameter. The delay from the scatter to the FDA-SAR antenna can then be calculated by

$$\Delta t = \frac{2r_a}{c_0} + \frac{2r_b}{c_0/\sqrt{\varepsilon_r}}. \tag{21}$$

This information can be used to compensate the bent effect for the PPC method.

B. IMAGING RESOLUTION AND SYSTEM PROCESSING GAIN

Suppose the baseband signal transmitted from each FDA antenna element is a chirp waveform with chirp rate k_r and pulse duration T_p. The range resolution is easily derived as

$$\rho_r^{\text{FDA}} = \frac{c_0}{2\left(|k_r T_p| + |(M-1)\Delta f|\right)}, \tag{22}$$

where $|k_r T_p|$ is just the baseband waveform bandwidth equal to the conventional SAR implying that the corresponding phase-array SAR resolution is $\rho_r^{\text{PA}} = \frac{c_0}{2|k_r T_p|}$, and $|(M-1)\Delta f|$ is the apparent signal bandwidth caused by the frequency offsets. It is known that a conventional SAR achieves an azimuth resolution $\rho_a = \frac{\lambda}{2\Delta\theta}$. Analogously, the FDA-SAR azimuth resolution is

$$\rho_a^{\text{FDA}} = \frac{\lambda}{2\Delta\theta_{\text{app}}}. \tag{23}$$

Due to the fact $\Delta\theta_{\text{app}} > \Delta\theta$, FDA-SAR achieves outperformed azimuth resolution than a phased-array SAR.

In a traditional classic SAR, the pulse compression gain will be $B_r T_p$, where B_r is the signal bandwidth and T_p is the signal pulse duration. Differently, since the FDA-SAR transmits the signals with slightly distinct carrier frequencies for each element, there will be coherent pulse compression gain loss due to the fact that the signals transmitted by all the FDA-SAR antenna elements are not totally overlapped in the frequency. The FDA-SAR coherent pulse compression gain can then be evaluated by $B_r \left(1 - \frac{\max_{m}\{\Delta f_m\}}{B_r}\right) T_p$. In addition, the transmit array gain is M and the receive array gain is N. Then the overall FDA-SAR gain is

$$\left[B_r \left(1 - \frac{\max_{m}\{\Delta f_m\}}{B_r}\right) T_p\right] \cdot M \cdot N, \tag{24}$$

which is almost the same as a phased-array radar with M transmitting elements and N receiving elements due to the fact that $\max_{m}\{\Delta f_m\} \ll B_r$ [22]. That is to say, FDA-SAR achieves improved imaging performance without significantly degrading the general array system gain.

C. CONSTRAINTS ON FREQUENCY OFFSETS

The closed-form (7) for a standard FDA is obtained by ignoring the m^2-related terms. It imposes the following constraints on the linearly increasing frequency offsets [19]

$$(M-1)^2 \frac{2\pi \Delta f d}{c_0} \le \frac{2\pi}{\eta}, \tag{25}$$

where $1/\eta$ sets the desired fraction of 2π. In the same time, to avoid target frequency decorrelation happen in each element, the frequency offsets are limited by [33]

$$\max_{m}\{\Delta f_m\} < \frac{c_0}{2\zeta \sin\theta}, \tag{26}$$

where ζ is the target length and $2\zeta \sin\theta$ is the length of the target projected along the radar boresight. This is a simplified model which is independent of the transmitted frequency. Moreover, to avoid signal decorrelation happen in each pulse, the frequency offsets are also limited by

$$\max_{m}\{\Delta f_m\} < \frac{1}{T_p}. \tag{27}$$

Note that the frequency offsets are mainly constrained by (25)-(27). As an example, suppose the following parameters: $\eta = 16$, $M = 16$, $d = 0.015m$, $M = 16$, $\xi = 5m$, $\theta = \pi/6$ and $T_p = 1\mu s$, according to (23) to (27), we then have $\Delta f \le 5.56$MHz, $\max_{m}\{\Delta f\} < 60$MHz and $\max_{m}\{\Delta f\} < 1$MHz, respectively. This implies that (27) plays more influence on the frequency offsets. In addition, the frequency offsets also have an influence on the FDA processing gain, as expressed in (22).

D. REFERENCE SIGNAL FOR MATCHED FILTERING

Matched filtering is an important step in the FDA-SAR processing. The essence is to adopt an appropriate reference signal. Consider the M-element FDA transmitted signal (10) for a single scatter. If we use the baseband waveform $u(t)$

as the reference signal, the corresponding matched filtering output will be

$$
\left[\sigma_1 s(t-\tau) \times e^{-j2\pi f_0 t} \right] \otimes u^*(t)
$$
$$
= \sigma_1 e^{-j2\pi f_0 r/c_0} \sum_{m=0}^{M-1} e^{j2\pi \frac{\Delta f_m r}{c_0}} \mathcal{A}(\tau, \Delta f_m), \qquad (28)
$$

where $\otimes$ is the convolution operator and $\mathcal{A}(\tau, f_d) = \int_{T_p} u(t-\tau)u^*(t)e^{j2\pi f_d t}\mathrm{d}t$ can be regarded as the waveform ambiguity function of $u(t)$, with f_d being the Doppler shift. The term $e^{-j2\pi f_0 t}$ is used to demodulate the received returns. It is noticed that, in this case, the frequency offsets Δf_m will introduce virtual Doppler shifts to the matched filtering output. Consequently, ghost imagery may be generated in the final FDA-SAR imaging results. To avoid this problem, we can use $\sum_{m=0}^{M-1} u(t)e^{j2\pi \Delta f_m t}$ instead of $u(t)$ as the reference signal for the FDA-SAR matched filtering in fast-time domain. Multichannel matched filtering algorithm can also be adopted.

E. LIMITATIONS
Besides varying apparent angle, FDA also exhibits interesting non-uniform plane wave (see Fig. 4). This is because that, for a given range, the FDA planes of constant phase and constant amplitude do not coincide, which generates differing orientations in the propagation. According to [26], the variation in FDA-SAR signal amplitude and phase may produce a set of apparent collection locations that are nonuniformly spaced and appear to alter the platform's actual flight path. An additional processing step is thus required between data collection and image focusing to formulate a mapping from the actual collection locations to the apparent SAR collection locations. The purpose is to match the phase history collected at the actual collection locations for the FDA-SAR transmitted signal.

In addition, the FDA-SAR assigned frequency offsets should operate precisely, but it is not an easy task in practical system implementation. Robust processing algorithm is necessary to address the effects of unideal frequency offsets.

V. TECHNICAL CHALLENGES AND FUTURE WORKS
FDA-SAR can adaptively update its range-dependent beam-pattern in both range and azimuth dimensions to suppress space-time-range-dependent interferences. However, in the FDA-SAR imaging algorithm, when the noise and interference are Gaussian, the unconstrained ML estimate of the signal covariance matrix is actually the sample variance matrix, but it is difficult to obtain the required covariance matrix of noise and interference in the FDA-SAR due to its range, angle and time-dependent response. This nonstationarity results in a limited amount of snapshot data avaiable for the processing that may be insufficient for an algorithm to coverage. A potential solution is to adopt subspace tracking algorithms such as projection approximation and fast approximated

power iteration [34]. In addition, a reiterative minimum mean square error algorithm was proposed in [35], which is capable of simultaneously adaptation in slow-time and fast-time to enhance sensitivity by suppressing Doppler and range sidelobes, but its large computation complexity due to multidimensional adaptivity must be significantly reduced for practical engineering applications. Reduced rank techniques can reduce the rank associated with the interference-plus-noise covariance matrix. Many rank reduction methods in the literature promise performance near or better than their full rank counterparts but with reduced sample support and computational load [36]. Particularly, several suboptimal fast-time STAP algorithms to suppress the direct-path and terrain scattered interferences, while preserving the final SAR quality, are introduced in [15]. Back projection algorithm was suggested in [26] by introducing a phase delay to compensate the propagation time between the apparent u_{app} and actual scene center u, but it is difficult to carry out two-dimensional interpolation, developing more efficient and effective algorithms is of great importance in future work.

As FDA is a rather new conceptual array technique, the basic implementation using monochromatic assumption and equally spaced elements is generally considered in the literature. Many more fertile areas remain for further exploration. Linearly increasing frequency increments and a uniform weighting vector are often assumed in existing FDA techniques. However, they may be not the best choice for specific applications. Strip-map FDA-SAR is considered in this paper, it is interesting to study arbitrary geometries and flight paths, such as spotlight SAR, circular SAR and interferometry SAR, etc. Two-dimensional FDA allows three-dimensional beam-steering in the azimuth and elevation dimensions, which pattern will be extremely unique and affords additional properties to develop operational strategies. Amplitude weighting can be employed to produce an FDA difference pattern, which may be also useful for rejecting multipath interferences, but more investigations are required.

Furthermore, directional modulation can be achieved for FDA. One simple approach is to divide the whole array into multiple subarrays, each of which is steered to a particular position. The frequency progression can be used across the subarrays, instead of across the elements as the basic FDA. Since the frequency progression produces both angle-dependent and time-variant beampattern, we can utilize the frequency progression in vertical dimension to alleviate the range layover effect, which is particularly beneficial in alleviating adverse three-dimensional SAR effects [26]. The essence is to construct an effective and efficient mapping between the actual collection location and the apparent collection location. This is an interesting future research topic.

Another future work is to optimize the frequency offsets. It is likely that the optimized frequency allocation is actually dependent on the physical scenarios. Several methods have been studied to optimally design the frequency offsets for

FDA and FDA-MIMO radars (see [22] and the references wherein), but no SAR related papers are found. It is expected that the increase in sample support data homogeneity can be considerably increased for the targets off-boresight in azimuth, as the isodop shape is better accentuated by the FDA beampattern. It is necessary to investigate possible benefits of adaptive frequency offsets control in the FDA-SAR systems.

Additionally, designing multichannel frequency-incremental synthesizer is an essence in FDA implementation. Wicks and Antonik [37] proposed a basic implementation scheme, which creates a predetermined frequency signal and this signal is mixed with multiples of the frequency offsets. Its main drawback is poor spectral purity caused by the mixers. Another implementation scheme is to use direct digital synthesizer to generate multichannel discrete sources, but at an expense of clock jitters and phase noise.

VI. CONCLUSION

FDA-SAR can exploit its unique properties of range-dependent beampattern to improve azimuth resolution and mitigate multipath interference and layover effects in SAR imaging. Through manipulation of FDA frequency offsets, target response at individual collection locations can be mapped to apparent collection locations. In doing so, the synthesized apparent aperture is longer than the actual aperture and thus, yields superior azimuth resolution. In this paper, we discussed the use of fast-time STAP to suppress undesired interferences for SAR subsurface imaging. The use of FDA range-dependent beampattern is suggested to mitigate the Doppler-range relationship by reducing the amount of isodops. Several technical challenges in signal processing aspects are also discussed. We aim to introduce this promising technique to the signal processing community so that more investigations can be facilitated.

REFERENCES

[1] S. Takahashi, K. Suzuki, T. Hanabusa, and S. Kidera, "Microwave subsurface imaging method by incorporating radar and tomographic approaches," *IEEE Trans. Antennas Propag.*, vol. 70, no. 11, pp. 11009–11023, Nov. 2022.

[2] C. Chen, Y. Su, Z. He, T. Liu, and X. Song, "Clutter mitigation in holographic subsurface radar imaging using generative adversarial network with attentive subspace projection," *IEEE Trans. Geosci. Remote Sens.*, vol. 60, 2022, Art. no. 5116214.

[3] Y. Zhou, N. Leng, Z. Wei, X. Ye, T. Yin, M. Bai, and X. Chen, "Learning-based subsurface quantitative imaging via near-field scanning microwave microscopy," *IEEE Trans. Microw. Theory Techn.*, vol. 70, no. 11, pp. 5008–5018, Nov. 2022.

[4] A. Aljurbua, H. N. Shaman, and K. Sarabandi, "A method to signal leakage cancellation in multistatic subsurface SAR imaging system," *IEEE Geosci. Remote Sens. Lett.*, vol. 9, pp. 173–190, 2022.

[5] C. Chen, C. Huang, Z. He, T. Liu, X. Song, and Y. Su, "Combining dual-frequency cancellation and sparse feature enhancement for nonplanar surface clutter mitigation in holographic subsurface imaging," *IEEE Trans. Geosci. Remote Sens.*, vol. 60, 2022, Art. no. 5111914.

[6] D. Comite, F. Ahmad, M. G. Amin, and T. Dogaru, "Forward-looking ground-penetrating radar: Subsurface target imaging and detection: A review," *IEEE Geosci. Remote Sens. Mag.*, vol. 9, no. 4, pp. 173–190, Dec. 2021.

[7] Y. Sun and J. Li, "Time-frequency analysis for plastic landmine detection via forward-looking ground penetrating radar," *IEE Proc.-Radar, Sonar Navigat.*, vol. 150, no. 4, pp. 253–261, Aug. 2003.

[8] K. Phaebua, T. Lertwiriyaprapa, S. Burintramart, and A. Boonpoonga, "The B-scan image simulation method of a ground-penetrating radar mounted on a drone using a high-frequency technique," *IEEE Access*, vol. 10, pp. 71656–71668, 2022.

[9] T. Jin and Z. Zhou, "Refraction and dispersion effects compensation for UWB SAR subsurface object imaging," *IEEE Trans. Geosci. Remote Sens.*, vol. 45, no. 12, pp. 4059–4066, Dec. 2007.

[10] L. Carin, N. Geng, M. McClure, J. Sichina, and L. Nguyen, "Ultra-wide-band synthetic-aperture radar for mine-field detection," *IEEE Antennas Propag. Mag.*, vol. 41, no. 1, pp. 18–33, Feb. 1999.

[11] Y. Chen, J. Li, H. Li, Y. Gao, S. Li, S. Chen, G. Guo, F. Wang, D. Zhao, K. Zhang, P. Li, K. Tan, and P. Du, "Revealing land surface deformation over the Yineng backfilling mining area, China, by integrating distributed scatterer SAR interferometry and a mining subsidence model," *IEEE J. Sel. Topics Appl. Earth Observ. Remote Sens.*, vol. 16, pp. 3611–3634, 2023.

[12] P. Paillou, S. Lopez, T. Farr, and A. Rosenqvist, "Mapping subsurface geology in Sahara using L-band SAR: First results from the ALOS/PALSAR imaging radar," *IEEE J. Sel. Topics Appl. Earth Observ. Remote Sens.*, vol. 3, no. 4, pp. 632–636, Dec. 2010.

[13] A. Elsherbini and K. Sarabandi, "Image distortion effects in SAR subsurface imaging and a new iterative approach for refocusing and coregistration," *IEEE Trans. Geosci. Remote Sens.*, vol. 52, no. 5, pp. 2994–3004, May 2014.

[14] J. R. Guerci, *Space-Time Adaptive Processing for Radar*. Norwood, MA, USA: Artech House, 2003.

[15] L. Rosenberg and D. A. Gray, "Constrained fast-time STAP for interference suppression in multichannel SAR," *IEEE Trans. Aerosp. Electron. Syst.*, vol. 49, no. 3, pp. 1792–1805, Jul. 2013.

[16] K. Greenewald, E. Zelnio, and A. H. Hero, "Robust SAR STAP via Kronecker decomposition," *IEEE Trans. Aerosp. Electron. Syst.*, vol. 52, no. 6, pp. 2612–2625, Dec. 2016.

[17] X. Li, M. Xing, X.-G. Xia, G.-C. Sun, Y. Liang, and Z. Bao, "Deramp space–time adaptive processing for multichannel SAR systems," *IEEE Geosci. Remote Sens. Lett.*, vol. 11, no. 8, pp. 1448–1452, Aug. 2014.

[18] P. Antonik, M. C. Wicks, H. D. Griffiths, and C. J. Baker, "Range-dependent beamforming using element level waveform diversity," in *Proc. Int. Waveform Diversity Design Conf.*, Jan. 2006, pp. 1–6.

[19] C. Cetintepe and S. Demir, "Multipath characteristics of frequency diverse arrays over a ground plane," *IEEE Trans. Antennas Propag.*, vol. 62, no. 7, pp. 3567–3574, Jul. 2014.

[20] H. C. So, M. G. Amin, S. Blunt, F. Gini, and W.-Q. Wang, "Introduction to the issue on time/frequency modulated array signal processing," *IEEE J. Sel. Topics Signal Process.*, vol. 11, no. 2, pp. 225–227, Mar. 2017.

[21] J. Xu, G. Liao, and H. C. So, "Space-time adaptive processing with vertical frequency diverse array for range-ambiguous clutter suppression," *IEEE Trans. Geosci. Remote Sens.*, vol. 54, no. 9, pp. 5352–5364, Sep. 2016.

[22] W.-Q. Wang, H. C. So, and A. Farina, "An overview on time/frequency modulated array processing," *IEEE J. Sel. Topics Signal Process.*, vol. 11, no. 2, pp. 228–246, Mar. 2017.

[23] I. G. Cumming and W. F. Wong, *Digital Processing of Synthetic Aperture Radar Data: Algorithms and Implementation*. London, U.K.: Artech House, 2005.

[24] D. Cerutti-Maori and I. Sikaneta, "A generalization of DPCA processing for multichannel SAR/GMTI radars," *IEEE Trans. Geosci. Remote Sens.*, vol. 51, no. 1, pp. 560–572, Jan. 2013.

[25] W.-Q. Wang, "Frequency diverse array auto-scanning beam characteristics and potential radar applications," *IEEE Access*, vol. 10, pp. 85278–85288, 2022.

[26] J. Farooq, "Frequency diversity for improving synthetic aperture radar imaging," Ph.D. dissertation, Air Force Inst. Technol., Wright-Patterson AFB, OH, USA, 2009.

[27] Y. Liu, H. Ruan, L. Wang, and A. Nehorai, "The random frequency diverse array: A new antenna structure for uncoupled direction-range indication in active sensing," *IEEE J. Sel. Topics Signal Process.*, vol. 11, no. 2, pp. 295–308, Mar. 2017.

[28] M. D. Zoltowski, "On the performance analysis of the MVDR beamformer in the presence of correlated interference," *IEEE Trans. Acoust., Speech, Signal Process.*, vol. 36, no. 6, pp. 945–947, Jun. 1988.

[29] Z. D. Zhu, Z. R. Ye, X. Q. Wu, J. Yin, and Z. S. She, "Super-resolution Range–Doppler imaging," *IEE Proc.-Radar, Sonar Navigat.*, vol. 142, no. 1, pp. 25–32, Feb. 1995.

[30] Y. Weidong and Z. Zhaoda, "SAR signal processing in subsurface radar," in *Proc. Int. Radar Conf.*, Beijing, China, 1996, pp. 301–304.

[31] J. Farooq, M. A. Temple, and M. A. Saville, "Application of frequency diverse arrays to synthetic aperture radar imaging," in *Proc. Int. Conf. Electromagn. Adv. Appl.*, Turin, Italy, Sep. 2007, pp. 447–449.

[32] T. G. Yitayew, L. Ferro-Famil, T. Eltoft, and S. Tebaldini, "Tomographic imaging of Fjord ice using a very high resolution ground-based SAR system," *IEEE Trans. Geosci. Remote Sens.*, vol. 55, no. 2, pp. 698–714, Feb. 2017.

[33] F. E. Nathanson, J. P. Reilly, and M. N. Cohen, *Radar Design Principles: Signal Processing and the Environment*. New York, NY, USA: McGraw-Hill, 1990.

[34] R. Badeau, B. David, and G. Richard, "Fast approximated power iteration subspace tracking," *IEEE Trans. Signal Process.*, vol. 53, no. 8, pp. 2931–2941, Aug. 2005.

[35] T. Higgins, "Waveform diversity and range-couple adaptive radar signal processing," Ph.D. dissertation, Dept. Elect. Eng. Comput. Sci., Univ. Kansas, Lawrence, KS, USA, 2011.

[36] J. S. Goldstein and I. S. Reed, "Reduced rank adaptive filtering," *IEEE Trans. Signal Process.*, vol. 45, no. 2, pp. 492–496, Feb. 1997.

[37] M. C. Wicks and P. Antonik, "Frequency diverse array with independent modulation of frequency, amplitude, and phase," U.S. Patent 7 319 427, Jan. 15, 2008.

WEN-QIN WANG (Senior Member, IEEE) received the B.E. degree in electrical engineering from Shandong University, Shandong, China, in 2002, and the M.E. and Ph.D. degrees in information and communication engineering from the University of Electronic Science and Technology of China (UESTC), Chengdu, China, in 2005 and 2010, respectively.

From March 2005 to 2007, he was with the National Key Laboratory of Microwave Imaging Technology, Chinese Academy of Sciences, Beijing, China. Since September 2007, he has been with the UESTC, where he is currently a Professor. From June 2011 to May 2012, he was a Visiting Scholar with the Stevens Institute of Technology, Hoboken, NJ, USA. From December 2012 to December 2013, he was a Hong Kong Scholar with the City University of Hong Kong, Hong Kong. From January 2014 to January 2016, he was a Marie Curie Fellow with Imperial College London, U.K. His research interests include signal processing for radar, communications, and microwave remote sensing. He is an Editorial Board Member of four international journals. He was a recipient of the Marie Curie International Incoming Fellowship, the National Young To-Notch Talent of the Ten-Thousand Talent Program Award, and the Hong Kong Scholar Fellowship.

● ● ●